

Characteristics of the On-Orbit Background of the Chandra X-ray Observatory High Resolution Camera

Michael Juda, R. Hank Donnelly, K. Tabetha Hole, Almus T. Kenter, Ralph P. Kraft, Stephen S. Murray, Deron O. Pease, Charles R. A. Wilton, and Martin V. Zombeck

Harvard-Smithsonian Center for Astrophysics, 60 Garden St, Cambridge, MA 02138

ABSTRACT

The Chandra X-ray Observatory (CXO) High Resolution Camera (HRC) is a microchannel plate (MCP) based X-ray detector with heritage from similar detectors flown on the *Einstein* and *ROSAT* missions. The HRC consists of two detectors in a common housing. Improvements from the previous instruments include: fabricating the MCP from "low-noise" glass (glass that contains a reduced level of radioactive isotopes) and surrounding the detector housing on five sides with an active coincidence detector. Both of these improvements help to maximize the X-ray signal to background noise ratio. The on-orbit background is dominated by cosmic ray and solar-wind particles. The temporal behavior of the background has two parts: a quiescent level and a flaring component. The quiescent level slowly changes with time and is correlated with the high-energy particle flux as measured by the Electron Proton Helium Instrument (EPHIN), the CXO radiation detector. The flaring component is associated with times of elevated low-energy particle flux, primarily from the Sun. A combination of on-board vetoing and filtering during ground processing provides a substantial rejection of the non-X-ray background.

Keywords: X-ray detector, microchannel plate, MCP, particle background, HRC, CXO

1. INTRODUCTION

The High Resolution Camera (HRC)¹ is one of two focal-plane instruments on-board the Chandra X-ray Observatory (CXO).² The HRC instrument contains two microchannel plate (MCP) based detectors in a common detector housing which share signal processing electronics. Similar MCP based detectors flew on the *Einstein* and *ROSAT* X-ray astronomy satellites. The two HRC detectors are not identical. One detector, the HRC-I, is optimized for wide-field imaging and consists of a pair of 100 mm by 100 mm MCPs. The other detector, the HRC-S, is optimized for readout of the Low-Energy Transmission Grating (LETG)³ and consists of three pairs of 100 mm by 30 mm MCPs arranged to form a long strip. The detector layout is shown in Fig. 1. The detector housing is surrounded by a coincidence detector of plastic scintillator read out by a photomultiplier tube. The CXO was launched into orbit three years ago and all systems, including the HRC, are operating well. Some highlights of the scientific results of the CXO are presented in other papers in these proceedings.⁴⁻⁸

One of the great strengths of the CXO is its ability to detect extremely faint sources. This strength comes about because the exceptional quality of the optic concentrates the X-rays from a point source into a small area on the detector. Of course, the source X-rays must be detected against whatever background level is present. The background will have contributions from a background internal to the detector (e.g. from radioactive isotopes within the detector itself), from an external particle background (e.g. cosmic rays), and from the diffuse X-ray background. The diffuse X-ray background is really a source, interesting in its own right, and cannot be reduced; however, any measures taken to reduce the other two contributors will improve the signal to noise for source detection.

Send correspondence to M. Juda, E-mail: mjuda@cfa.harvard.edu

Copyright 2003 Society of Photo-Optical Instrumentation Engineers.

This paper was published in SPIE Proceedings 4851, 112 and is made available as an electronic reprint with permission of SPIE. One print or electronic copy may be made for personal use only. Systematic or multiple reproduction, distribution to multiple locations via electronic or other means, duplication of any material in this paper for a fee or for commercial purposes, or modification of the content of the paper are prohibited.

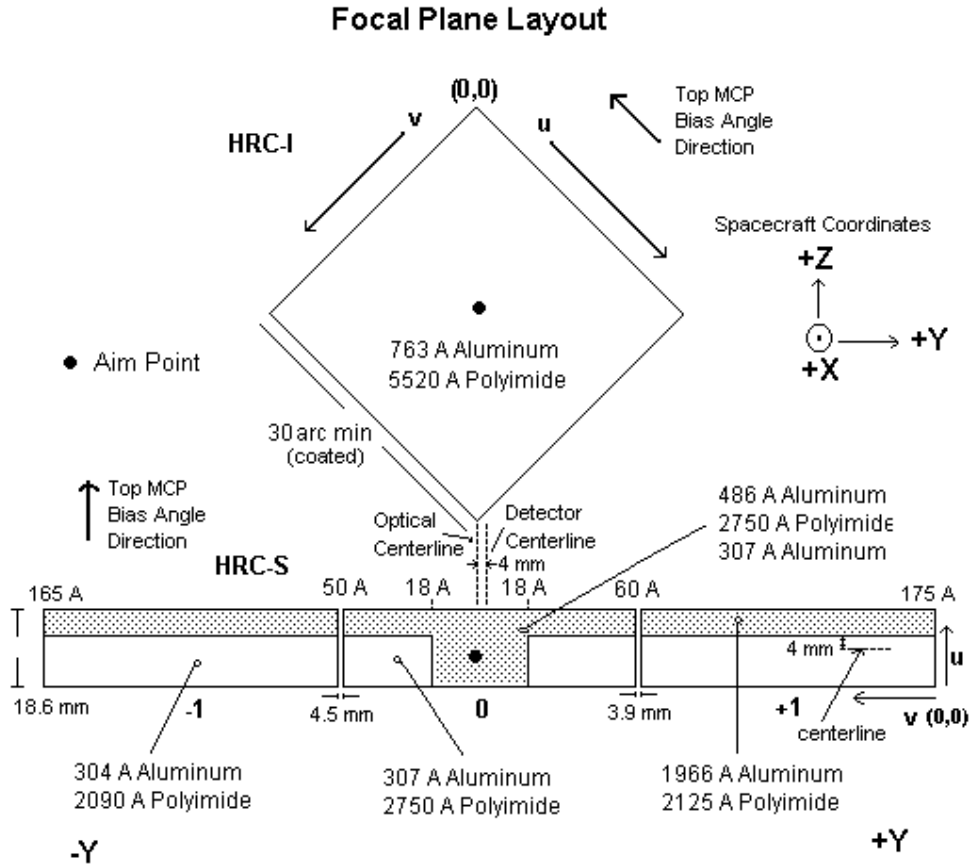


Figure 1. Layout of the HRC focal plane.

The HRC has several improvements over the detectors from *Einstein* and *ROSAT* that help to reduce the background or improve our ability to identify background events. The HRC MCPs are made from glass with a reduced content of radioactive isotopes^{9,10}; this results in a low internally generated background, typically less than $0.1 \text{ counts s}^{-1} \text{ cm}^{-2}$. The coincidence signals from the plastic scintillator that surrounds the detector housing are used to flag MCP events that have a timing overlap with them; these events are presumably due to cosmic rays that penetrated both the detector MCPs and the scintillator. On-board processing of the flagged events can be terminated, rejecting these events from the telemetry stream, or the flagged events can be rejected during ground processing of the telemetered data. Unfortunately, while the coincidence signal operates as expected with the HRC-I, a difference in the shape of the signals from the HRC-S MCPs renders the coincidence timing ineffective. Lastly, the HRC telemeters more raw information about each event, permitting us to examine characteristics of the charge distribution for the event. We can use these characteristics to flag events that are likely to be due to cosmic rays.¹¹

The CXO also carries a particle detector, the Electron, Proton, Helium Instrument (EPHIN),¹² that is primarily used to monitor the radiation environment for the protection of the science instruments. The EPHIN provides rates in several particle-energy channels: including electrons in four energy ranges covering 0.25-10 MeV, protons in four energy ranges covering 5.0-53 MeV, and an Integral channel that measures electrons with energies greater than 8.7 MeV and protons and nuclei with energies greater than 53 MeV/nucleon. The EPHIN Integral channel provides a good measure of the cosmic-ray flux.

In this paper we describe the characteristics of the HRC background that we have observed over the first

three years of CXO operations. In Sect. 2 we cover both the long- and short-term temporal behavior in the observed background and relate it, where possible, to other measures of the background environment. In Sect. 3 we discuss the spatial distribution of the background in the HRC-I and the effects of event screening; a similar discussion for the HRC-S appears in Sect. 4.

2. TEMPORAL VARIATION

Early in the mission it was recognized that the background in both of the focal-plane science instruments exhibited flaring above a quiescent level. There are several reasons to expect time-variability in the background. Variation in the solar magnetic field over the 11-year solar cycle modulates the cosmic ray flux at the Earth. The CXO was placed in a highly elliptical orbit that passes into and out of the Earth’s trapped particle belts. While the science instruments are stopped from collecting data in the belts in order to protect them from the high flux of particles, the environment on the fringes of the belts, where they do take data, is not constant. The CXO mission started just before solar maximum; increased solar activity creates variability in the CXO particle environment in several ways: Solar flares and coronal-mass ejections (CMEs) can send clouds of particles toward the Earth and the CXO. Finally, the flares and CMEs impacting the Earth’s magnetosphere modifies the shape and particle population of the Earth’s radiation belts.

2.1. Quiescent Level

The detector internal background and the cosmic-ray induced background provide a quiescent level for the background that can be expected to vary only slowly in time. The internal background can change as the detector and the surrounding material get activated by high-energy particles over time.¹³ The cosmic-ray flux varies over the solar cycle, as mentioned above. Figure 2 shows a comparison of the EPHIN Integral channel flux to the HRC-I total event rate as a function of time. The EPHIN operates continuously; times when the CXO was in the Earth’s radiation belts have been removed from the EPHIN data by selecting times when the distance from the Earth’s center was greater than 80,000 km. The EPHIN data points are daily averages. Most of the EPHIN points lie along a curve that varies smoothly in time; the other points are days affected by hard solar flares. The HRC does not collect data all the time. In order to minimize the risk to the HRC detectors, the MCP HV is only raised to the operating level at the start of an HRC observation and only for the selected detector (HRC-I or HRC-S). Typically the MCP HV is left at the operating level until either the other HRC detector is used or the CXO is about to enter the Earth’s radiation belts. If there are no HRC observations in a given orbit the MCP HV is not raised to the operating level. In addition to the data for individual X-ray events the HRC data contains scalars that report the MCP total trigger rate (total rate) and the rate of triggers that pass on-board event quality checks (valid rate); the rate in the coincidence detector is reported as well. Most of the HRC-I data points in Fig. 2 are the average total rate for individual HRC-I pointed observations; a few points, indicated by diamond symbols, are averages taken when the HRC-I was not viewing the sky (i.e. during ACIS observations). The minimum of the HRC-I rate as a function of time displays the same general shape as the EPHIN Integral channel data; MCP total rates above this trend are expected due to observations of bright X-ray sources and from flaring background. The HRC-S MCP total event rate shows a similar behavior.

A more direct comparison of the EPHIN Integral channel flux and the HRC-I MCP rate is shown in Fig. 3. Here the EPHIN data have been averaged over the times of the individual HRC observations. The bulk of the data points lie along a line and the points from observations that contain bright X-ray sources or have a contribution from the flaring background lie above the line. We can use the fact that the HRC-I is routinely operated such that the MCP events that are coincident with events in the scintillator are rejected on-board (i.e. they are not “valid” events) to select observations that have a minimal contribution from X-ray sources or flaring background. Figure 4 is a scatter-plot comparing the HRC-I MCP valid event rate to the total event rate. As indicated by the line drawn from the origin, there appears to be a lower limit on the ratio of the valid rate to the total rate, with a value of ~ 0.23 ; celestial X-rays add equally to the total and valid rate resulting in trends away from this ratio with a slope of 1.0. We interpret this lower limit on the ratio as representative of the quiescent value. When the HRC-I is not viewing the sky it does see any celestial X-ray sources, we see no evidence for the flaring background, and the ratio of the valid event rate to the total event rate is higher at ~ 0.27 . It is possible that when the HRC is not in the viewing position, the additional structure in front of the

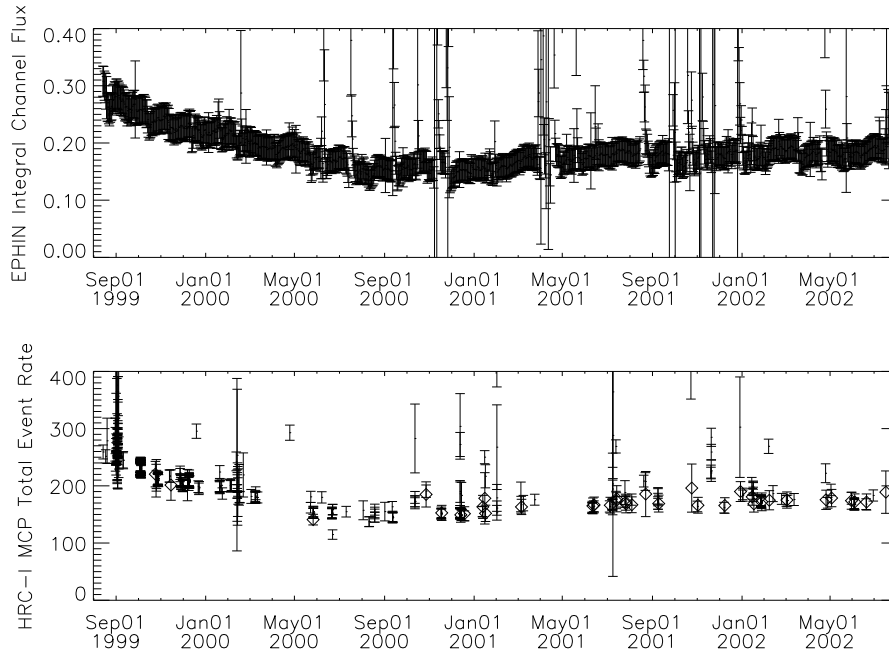


Figure 2. EPHIN Integral channel flux (particles $\text{cm}^{-2} \text{s}^{-1} \text{sr}^{-1}$) and HRC-I MCP total rate (counts s^{-1}) as a function of time. The EPHIN data points are daily averages for spacecraft geocentric distances greater than 80,000 km. HRC-I data are averages over individual pointed observations (no symbol) or over times when the HRC-I was collecting data but not viewing the sky (diamonds).

MCPs reduces the energies of the incident particles enough that they do not reach the coincidence detector; as a result, fewer particle events are rejected on-board. By selecting only those observations for which the valid/total ratio is within a narrow band around 0.23, we can be reasonably confident of having HRC-I MCP total event rates that reflect the quiescent background level. The best fit line to this subset has a slope of 785 ± 33 (counts s^{-1})/(particles $\text{cm}^{-2} \text{s}^{-1} \text{sr}^{-1}$) and an intercept of 34 ± 10 counts s^{-1} . This fit is plotted in Fig. 3. This relationship will allow us to estimate the quiescent contribution to the background given the EPHIN Integral channel flux during the observation.

There are two issues that make doing a similar analysis for the HRC-S more difficult. First, because of differences in the shapes of the signals coming from the HRC-S MCPs relative to the HRC-I, the HRC-S double-counts events with large MCP signal amplitudes. The amplitude threshold for an event to be double-counted is different for each of the three MCP segments. While the trend in the reported rates is correct the detailed information is not. Second, the HRC-S can be operated in several different modes in which different detector areas are active. Analysis can be done on subsets taken in the different configurations, taking into account the differences in the areas. Given these issues, the behavior in the quiescent background is essentially the same in the HRC-S as in the HRC-I.

2.2. Flaring behavior

Time variability in the rates that occurs over time scales from seconds to hours is generally referred to as flaring. The causes for this flaring include: impulsive solar flares, CMEs, and moving through the fringes of the Earth's radiation belts. Impulsive solar flares can generate hard protons that are detected in the EPHIN Integral channel and cause an increase in the HRC MCP total rate. When a CME arrives at Earth we frequently see an increase in the variability of the HRC MCP total and valid rates, particularly when the CXO is near the

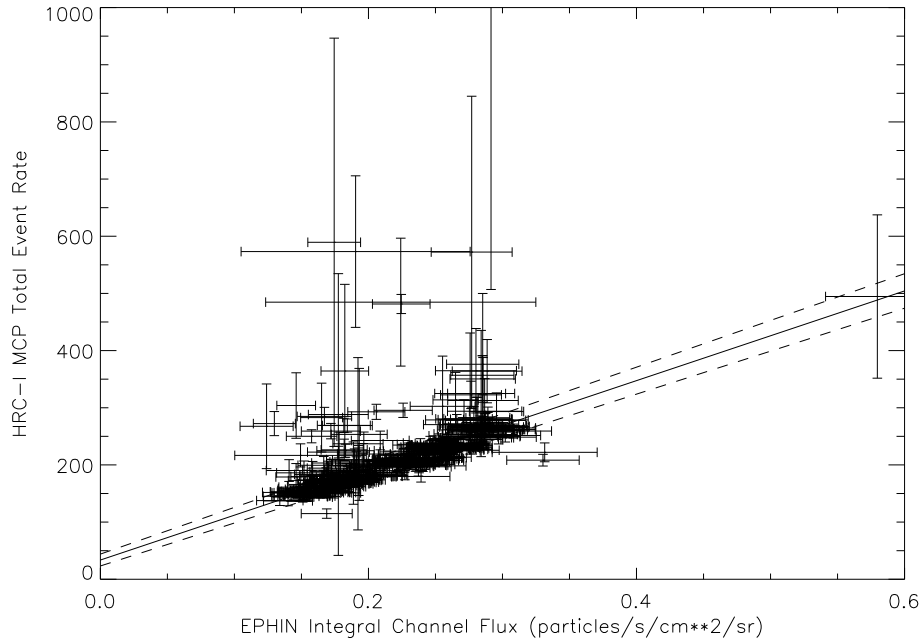


Figure 3. HRC-I MCP total event rate versus EPHIN Integral channel flux. The solid line is a fit to a subset of the data for which the HRC-I rate is less affected by the observed X-ray sources or flaring in the background. The dashed lines show the 1-sigma limits on the fit.

Earth’s radiation belts. However, frequently there is flaring in the rates that occurs without any clear causative event.

Figure 5 shows an example of flaring in the HRC-S data from early in the mission. The variability in the rate is not related to the X-ray sources in the field of view. Also shown in the plot are the fluxes measured by EPHIN in the lowest electron channel, E150 (0.25-0.7 MeV); the lowest proton channel, P4 (5.0-8.3 MeV); and the Integral channel. Of the EPHIN channels, the E150 channel shows the greatest variability during this time, although some variation is evident in the P4 channel. Unfortunately, there is no detailed correlation between the variation in the HRC-S total rate and the EPHIN E150 or P4 channels. We have been unsuccessful in observing detailed correlations between the flaring background in the HRC-I or HRC-S and any of the EPHIN particle channels for other intervals of flaring but these times of flaring are frequently accompanied by elevated rates in the lowest energy EPHIN channels. Particle detectors on other spacecraft can give us an idea of the general particle environment around the Earth. Data from the Advanced Composition Explorer (ACE) spacecraft showed elevated fluxes of protons in the 0.05-1.0 MeV range before and during the time plotted in Fig. 5 and such an association is common among the time intervals that exhibit flaring MCP rates. As we discuss in Sect. 4, the spatial distribution of the background in the HRC-S suggests that most of this flaring component is due to protons with energies well below the EPHIN detection threshold of ~ 5 MeV.

3. HRC-I SPATIAL DISTRIBUTION

There is no reason to expect that the spatial distribution of the background across HRC-I to be uniform. Localized “hot-spots” may be present, caused by defects in the MCP or by the structure holding the MCP that provides sites for field-emission of electrons. There could be variations in the detection sensitivity of the MCPs to the cosmic rays due to detector gain variations. The structure surrounding the MCPs might create variations in the cosmic ray flux across the MCPs or in the fraction of events that also result in signals in the scintillator

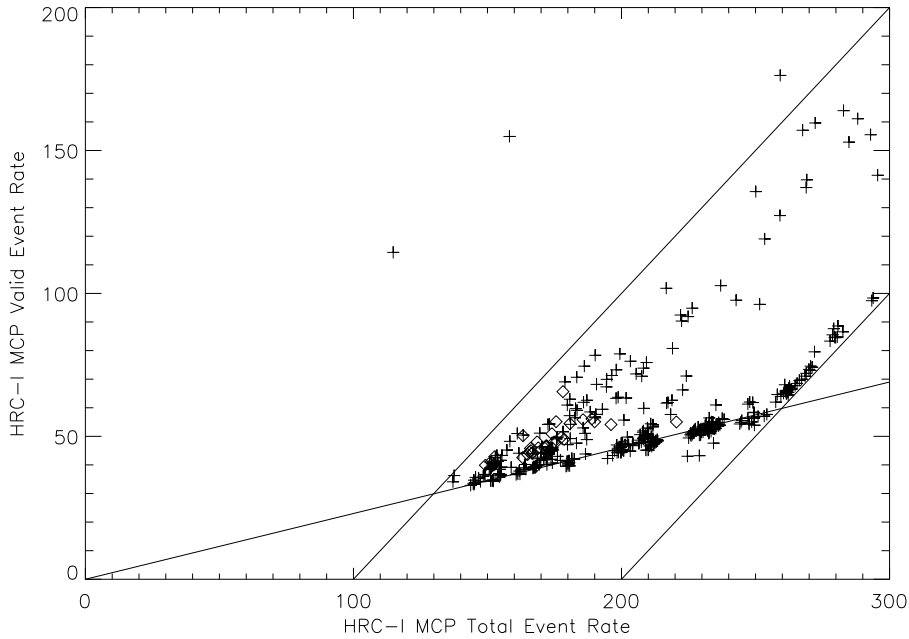


Figure 4. HRC-I MCP valid event rate versus the total event rate. Plus symbols mark data from sky observations and diamonds mark data from non-sky-viewing times; error-bars are omitted for clarity. The straight line from the origin was set to go through the lower-limit of the valid/total ratio and has a slope of 0.23. The other two straight lines have a slope of 1.0 to indicate how events that add to both the total and valid rates would trend off the ratio.

detector. An understanding of spatial variations in the background is as critical as an understanding of the temporal variations when it comes to modeling the detector background.

The best data on the spatial distribution of the HRC-I internal background come from laboratory measurements made before launch. If the isolated “hot-spots” and the perimeter of the active area are ignored the observed spatial distribution of the background is uniform at a level of 3×10^{-6} counts s^{-1} arcsec $^{-2}$. This value is really an upper limit to the internal component since some of this “internal” background is likely to have been generated by atmospheric muons and the radioactive decay of building materials near the detector.

On-orbit the observed background is several times larger than that measured in the laboratory. Because the HRC-I MCP total rate observed at launch was above the maximum rate at which we could telemeter all the event data (telemetry saturation), the HRC was commanded to reject the MCP events that were coincident with signals from the scintillator detector. Figure 6a is an image of the background taken when the HRC-I was not viewing the sky; Fig. 6b is an image of the same data-set after applying standard filters in ground processing based on event quality.¹¹ Before filtering, the distribution is maximum in the center of the detector and rolls off toward the edges; this pattern is similar to that in the detector gain. This centrally peaked distribution lies on top of a negative gradient from the lower-left to upper-right in the image; this gradient is the dominant pattern in the filtered image. The orientation of this gradient is consistent with the possibility that the HRC detector housing door may block or modify some fraction of the particle flux.

While we routinely operate the HRC-I with on-board rejection of the MCP events that are coincident with scintillator signals, we have performed an observation where this wasn’t the case. When we select from this observation only the events that were flagged as coincident with scintillator signals to form an image, we see a distribution that is centrally peaked, similar to the portion that is filtered out in the background images discussed above. The event quality filters were designed to eliminate events that were likely to be caused by cosmic rays and this suggests that they function as expected. The image of coincidence events also shows a

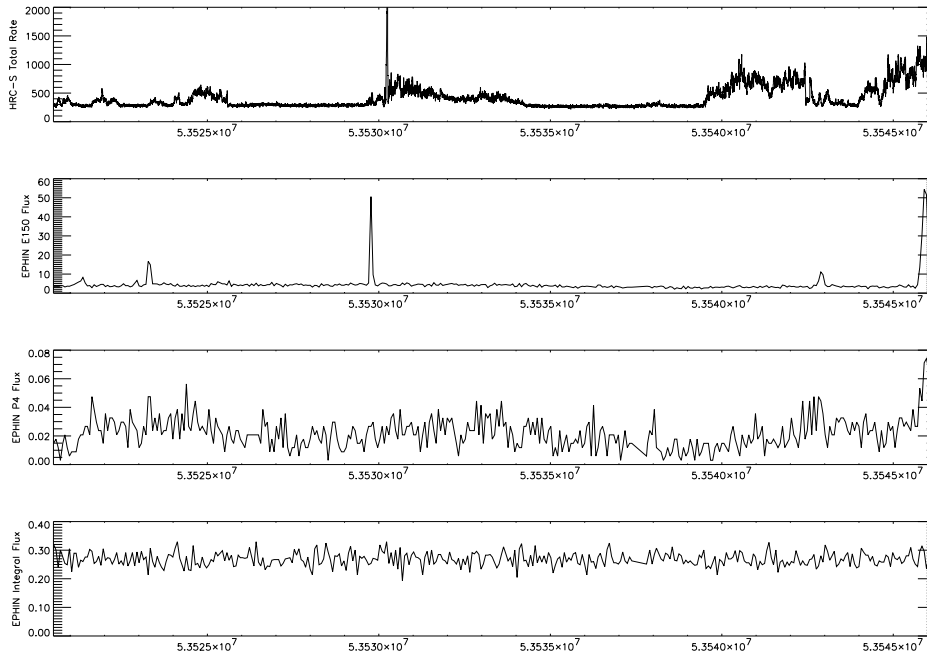


Figure 5. An example of flaring in the HRC-S total event rate as a function of time. Fluxes measured in the lowest EPHIN electron and proton channels as well as the Integral channel are also plotted.

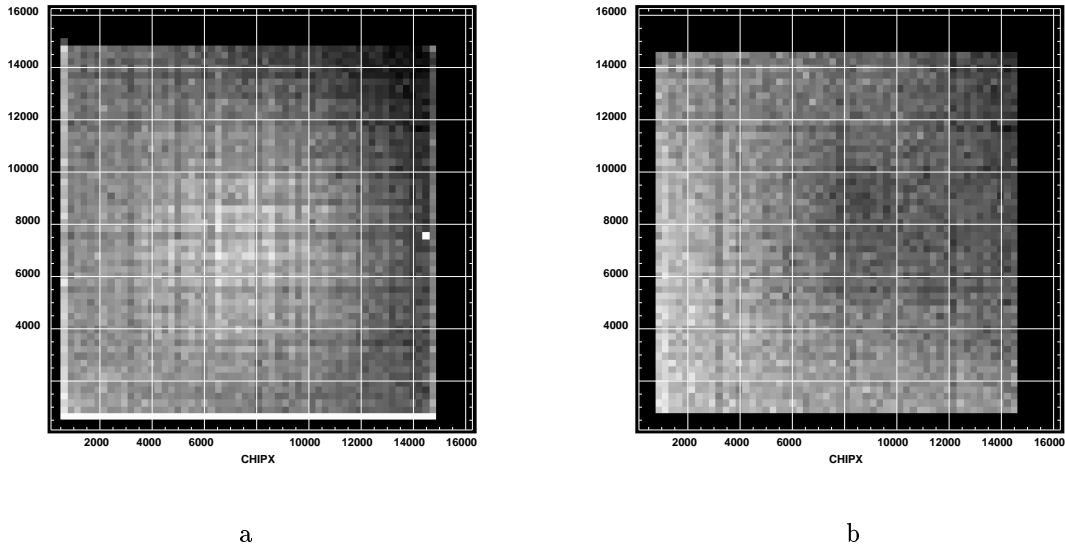


Figure 6. Grey-scale images of the HRC-I background spatial distribution observed when the HRC-I was not viewing the sky: a) unfiltered, b) filtered. The image is displayed in “CHIP” coordinates, which are aligned with the HRC-I detector axes; image cells are 256 detector pixels (33.7 arcsec) on a side. The grey-scale range is zero-suppressed so the the variation is enhanced; the grey-scale range is 0.8-1.2 times the background mean for each image.

suggestion of a gradient that underlies the central peaking but which trends in the opposite sense as that shown in Fig. 6b. Such opposing gradients would be expected if the HRC door degraded the particle energies enough that some of the particles could not penetrate to the scintillator after reaching the MCPs.

Using data when the HRC-I is not viewing the sky has the advantage that the background does not include X-rays from celestial sources or contamination from the flaring background; as such, it is hoped that these images reflect the spatial variation of the quiescent background. However, there is a possibility that the spatial distribution of this quiescent component changes between the viewing position and non-viewing position. Indeed, as discussed in Sect. 2.1, the ratio of the HRC-I MCP valid rate to the total rate changes between the two positions. We have looked for such a variation by selecting a set of HRC-I calibration observations of the star AR Lac, where the pointing direction was varied to place AR Lac at different locations on the detector. For each observation, events within a circular region centered on AR Lac were rejected; the size of the circular region had a radius of at least ~ 7.9 arcsec and was adjusted based on the off-axis angle of the observation; times that appeared to be affected by flaring background were rejected as well. Note that this process for “cleaning” the observations does not remove all the celestial X-rays. In particular, the cleaning process can leave X-rays from AR Lac that lie outside the extraction radius; a visual examination of the background image created from the AR Lac observations showed enhancements that followed the pattern of the different pointing directions. We compared the background spatial distributions from the non-viewing data and the AR Lac data and found differences that were consistent with an incomplete removal of celestial X-rays; so as a first approximation the non-viewing data does represent the spatial distribution of the HRC-I quiescent background when viewing the sky.

4. HRC-S SPATIAL DISTRIBUTION

We can expect a spatial variation in the HRC-S background for most of the same reasons given for variations in the HRC-I background (the exception being that coincidences of events with a signal in the scintillator do not occur). An additional reason for spatial variation, that is important for lower energy particles, is created by variations in the thickness of the material in the UV/ion shield, an aluminized-polyimide film in front of the MCPs. One complication in understanding the spatial distribution of the HRC-S background is the fact that the HRC-S is operated in different modes, selecting different active areas, in order to reduce the quiescent valid event rate to on the order of half the telemetry saturation value. Two modes receive the bulk of HRC-S observing time: the default spectroscopy configuration that selects a strip of about one half the width of the HRC-S active area, along the entire length; and the high-resolution timing mode that uses only triggers from the center MCP segment with the trigger level slightly higher than the default value. A third mode has been used for many calibration observations that also selects the central MCP as the active region but keeps the default trigger level. Both sky-viewing and non-sky-viewing data are available for each of these modes. Unfortunately, in the most heavily used mode, the one for LETG spectroscopy, when viewing the sky the dispersed spectrum lies in the area in which we are most interested in the background. We examine data from each of these modes below.

4.1. Default Spectroscopy Mode

The default configuration for the HRC-S uses a hardware “edge-blanking” function to reject events that occur outside of a defined rectangular region. For spectroscopy, the rectangular region runs the entire length of the detector but only covers a strip of half the width down the center. Figure 7 shows an image of the background from non-viewing data. Also shown are images from data taken from the observation whose light curve was plotted in Fig. 5, where the data was sub-divided into low-flaring and high-flaring intervals. The sky observation data is useful in that the LETG was not inserted, so there are no diffracted X-rays. While the on-axis source, Capella, has been removed from the data, other sources have not; there is evidence for an off-axis source present at $V \approx 37000$. No event quality filters have been applied to these data. The spatial distributions of the non-sky-viewing and the low-flaring images are similar, with higher spots near the centers of each of the segments. One difference between these two images is that the wing segments in the low-flaring data are slightly brighter compared to the center segment than in the non-viewing data. This brightening of the wing segments is even more pronounced in the high-flaring data. In addition, the center segment of the high-flaring data shows an

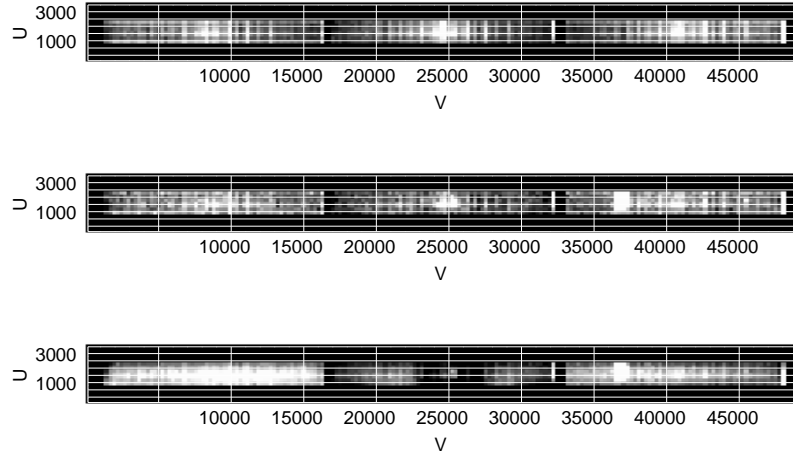


Figure 7. Images of the HRC-S background in the default spectroscopy mode. Top: non-sky-viewing, Middle: low-flaring, Bottom: high-flaring. The images are displayed in the HRC-S coordinates with image cells 256 detector pixels (33.7 arcsec) on a side. Grey-scale range is 0.8-1.2 of the field mean in each image.

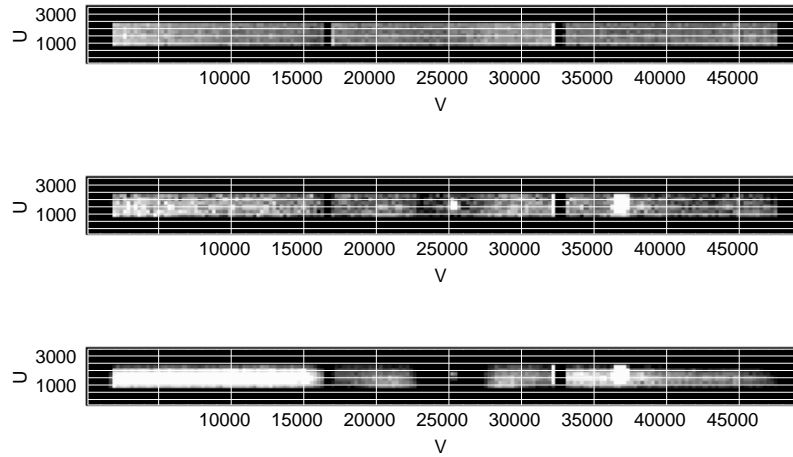


Figure 8. Images of the HRC-S background in the default spectroscopy mode after the standard event quality filters have been applied. Top: non-sky-viewing, Middle: low-flaring, Bottom: high-flaring. The images are displayed in the HRC-S coordinates with image cells 256 detector pixels (33.7 arcsec) on a side. Grey-scale range is 0.8-1.2 of the field mean in each image.

abrupt dimming in the central third. These variations in brightness of the background in the high-flaring data match locations where the thickness of the UV/ion shield changes. Figure 8 displays the same three data sets after the standard event quality filters have been applied. After filtering the peaking toward the centers of the segments has been removed, similar to the result with the HRC-I, and the shadows cast in the flaring component by the thicker parts of the UV/ion shield have become more apparent. The flaring component in the background is substantially attenuated by the additional thickness of 486\AA ($\sim 12 \mu\text{g}/\text{cm}^{-2}$) of aluminum. For a flaring background composed of protons, the significant attenuation by such a small mass implies energies

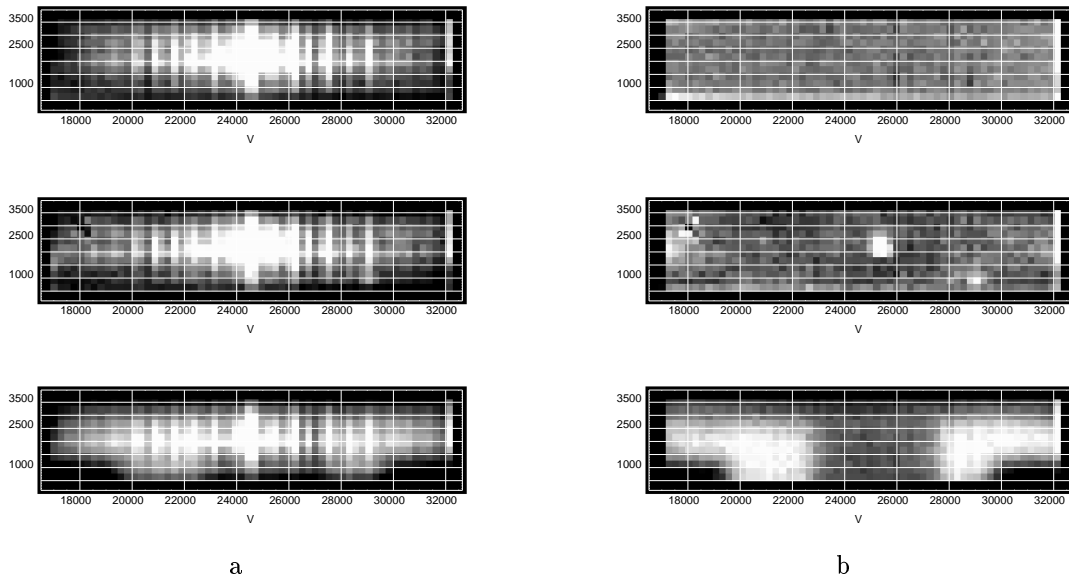


Figure 9. Grey-scale images of the HRC-S background spatial distribution taken in the high-precision timing mode: a) unfiltered, b) filtered. The top images are from data taken when the HRC-S is not viewing the sky, the middle images are from an observation with no flaring, and the bottom images are from an observation contaminated by flaring. The images are displayed in the HRC-S coordinates; image cells are 256 detector pixels (33.7 arcsec) on a side. The grey-scale range is zero-suppressed so the the variation is enhanced; the grey-scale range is 0.75-1.25 times the background mean for each image.

well below 1 MeV.

4.2. High-precision Timing Mode

The HRC-S is used to perform observations where high-precision timing is a key objective by setting it into a mode where the hardware shunts the signals from the two wing segments to ground (“Imaging” mode); thus, only the center segment should produce triggers. In addition, the trigger threshold is raised slightly so that extremely large signal in the wing segments cannot generate spurious triggers. Figure 9 shows background images taken while the HRC-S was in the high-precision timing mode. Images are shown from data taken when the HRC-S was not viewing the sky, from an observation that appears to be free of flaring, and from an observation that was contaminated by flaring. Both raw and filtered images are shown. For the sky observations, X-rays from the target and a few of the brightest sources have been removed from the data but celestial X-rays are still present. Once again, the spatial distribution peaks toward the center of the MCP in the unfiltered data and this peaking is removed by the event quality filtering. After filtering, the spatial distribution in the non-sky-viewing data is smooth and fairly flat. There is more variation in the non-flaring sky observation but a significant portion of the variation may be due to celestial X-rays. The spatial distribution of the flaring-contaminated sky observation once again shows the shadow of the thicker aluminum in the UV/ion shield as well as a shadow cast by the reflectors of the high-energy suppression filter (HESF).¹⁴ The background in the HESF shadow is lower than in the thick aluminum area, indicating that it probably blocks all of the flaring component

4.3. Center Segment Mode

The center segment of the HRC-S can also be selected as the active area using the “edge-blanking” function that is used to define the default spectroscopy region. There is no difference between using edge-blanking or imaging mode in which events get selected as good. However, the high-precision timing mode uses a higher trigger threshold to detect events and this can lead to differences in their background spatial distributions. A difference

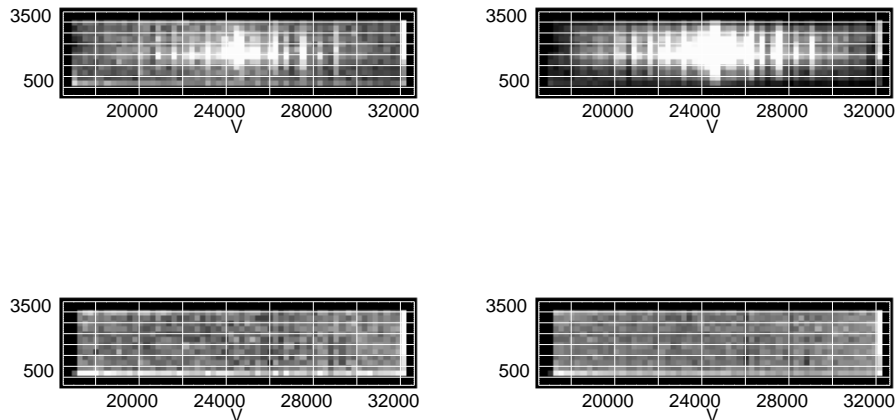


Figure 10. Comparison of backgrounds between the edge-blanking selected center segment mode and the high-precision timing mode from non-sky-viewing data. Left-side images are for the edge-blanking, right-side are high-precision timing; top images are raw, bottom are filtered. The images are displayed in HRC-S coordinates; image cells are 256 detector pixels (33.7 arcsec) on a side. The grey-scale range is zero-suppressed so the the variation is enhanced; the grey-scale range is 0.75-1.25 times the background mean for each image.

in the spatial distributions exists for the raw data as can be seen in Fig.10. The high-precision timing mode data shows a much larger variation from the detector edges to the center (more peaking toward the center) than in the edge-blanked mode; this is most likely caused by position dependent variations in the size of the trigger signal induce by cosmic rays in the MCP segment. After using the event quality filter on the edge-blanked data, the spatial distribution is indistinguishable from the comparable data from the high-precision timing mode. When an observation is contaminated by a flaring background, the same shadows from the thicker aluminum of the UV/ion shield and the HESF appear.

5. CONCLUDING REMARKS

There are some clear trends observed in the temporal and spatial behavior of the measured HRC backgrounds; unfortunately, we don't have independent predictors for all of these trends. One key reason for characterizing the behavior of the background contributors is so that we can develop models or recipes for estimating the background that was seen in any given observation. We are currently working on techniques for modeling the contribution of the quiescent background to the background using its observed temporal and spatial characteristics. Because of its unpredictable time behavior, it is likely that different methods will be required for modeling the flaring background. When their development is complete, the techniques and any required calibration data will be released to the CXO observer community for their use in analyzing observations.

The work presented here is a start at characterizing the on-orbit background observed by the HRC and several areas merit further investigation. One key area for continuing work is in searching for and characterizing any differences in the flaring component of the background. The search for differences could be based on parameters such as: the observed rate in the flaring component; proximity of the CXO to the Earth's radiation belts; the level of activity in the lowest energy EPHIN channels; time since the last CME; or particle environment as measured by other spacecraft. With continuing observations, the statistics that we obtain for the various components and configurations will improve; it may then be that we can distinguish differences where we currently cannot. Since we are only part of the way through a solar-cycle and we see evidence for variation in the total rate in the

detectors, we should expect additional rate changes in the future. It is conceivable that the spatial distribution of the quiescent background may show difference between solar-minimum and solar-maximum. Clearly there is more work ahead of us.

ACKNOWLEDGMENTS

This work was supported by NASA contract NAS8-39073 to the Chandra X-ray Center.

REFERENCES

1. S. S. Murray, and J. H. Chappell, *The Advanced X-Ray Astrophysics Facility High Resolution Camera*, *Proc. SPIE* **597**, 279, 1986.
2. M. C. Weisskopf, S. L. O'Dell, R. F. Elsner, and L. V. van Speybroeck, *Advanced X-Ray Astrophysics Facility (AXAF): an overview*, *Proc. SPIE* **2515**, 312, 1995.
3. A. C. Brinkman, J. J. van Rooijen, J. A. M. Bleeker, J. H. Dijkstra, J. Heise, R. Mewe, F. Paerels, & P. A. J. de Korte, *Low Energy Transmission Grating Spectrometer (LETGS) for AXAF*, *BAAS*, **17**, 865, 1985.
4. M. C. Weisskopf, *Three years of operation of the Chandra X-ray Observatory*, *Proc. SPIE* **4851**, 2002.
5. S. S. Murray, *Science highlights from Chandra HRC program*, *Proc. SPIE* **4851**, 2002.
6. G. P. Garmire, M. W. Bautz, J. A. Nousek, and G. R. Ricker, Jr., *Advanced CCD imaging spectrometer (ACIS) instrument on the Chandra X-ray Observatory* *Proc. SPIE* **4851**, 2002.
7. K. A. Flanagan, *Probing the cosmic X-ray laboratory with the Chandra HETGS*, *Proc. SPIE* **4851**, 2002.
8. M. Mendez, *LETGS: instrument status and science highlights*, *Proc. SPIE* **4851**, 2002.
9. M. R. Garcia, J. H. Chappell, S. S. Murray, W. B. Feller, and G. W. Fraser, *Low Noise Microchannel Plate Detectors for X-ray Astronomy*, *Proc. SPIE* **1140**, 101, 1989.
10. J. H. Chappell, R. K. Martin, S. S. Murray, and M. V. Zombeck, *Background Reduction in Microchannel Plates*, *Proc. SPIE* **1344**, 176, 1990.
11. S. S. Murray, J. Chappell, A. Kenter, M. Juda, R. Kraft, M. Zombeck, G. Meehan, G. Austin, and J. Gomes, *Event Screening for the Chandra X-Ray Observatory High Resolution Camera (HRC)*, *Proc. SPIE* **4140**, 144, 2000.
12. R. Muller-Mellin, *et al.*, *COSTEP - Comprehensive Suprathermal and Energetic Particle Analyser*, *Solar Physics* **162**, 483, 1995.
13. K. L. Dietz, *et al.*, *Shielding simulations for the Advanced X-ray Astrophysics Facility (AXAF)*, *Proc. SPIE* **2518**, 107, 1995.
14. S. S. Murray, *et al.*, *AXAF High-Resolution Camera (HRC): calibration and recalibration at XRCF and beyond*, *Proc. SPIE* **3114**, 11, 1997.